Numerical Analysis of Hyperelastic Material Behavior Towards Shape-Adjustable Sensor Devices

Nadine Philippin[1,2,*], Alexander Frey[3] and Ingo Kuehne[1]

[1] Heilbronn University of Applied Sciences, Kuenzelsau, BW, Germany
[2] Technical University of Munich, Professorship of Microsensors and Actuators, Munich, BY, Germany
[3] Augsburg Technical University of Applied Sciences, Augsburg, BY, Germany
*nadine.philippin@hs-heilbronn.de

In recent years, conventional rigid and planar sensor devices are gradually substituted by flexible and stretchable alternatives. This paradigm shift along with the availability of enhanced functional materials and novel fabrication techniques has paved the way to entirely new applications, particularly in the field of personalized health monitoring. To meet the manifold requirements of shape-adjustable sensors such as an adequate durability and improved hysteresis characteristics, an in-depth understanding of the relating hyperelastic material behavior is indispensable. In this paper, the numerical analysis of stretchable thermoplastic polyurethane (TPU) substrates with integrated copper traces serving as resistive and capacitive sensor elements is presented. Fundamentals of phenomenological hyperelastic material models with emphasis on the 5 parameter Mooney-Rivlin approach to describe the material behavior of TPU best possible are discussed in a first instance. Capabilities for shape optimization of embedded copper traces are additionally studied by means of COMSOL Multiphysics® in consideration of TPU strain rates up to 60%. Based on these findings, first designs for shape-adjustable resistive and capacitive sensor devices are successfully realized and modeled by FEM simulations.

Keywords—**hyperelasticity, Mooney-Rivlin model, sensors, shape-adjustable, thermoplastic polyurethane (TPU)**

I. INTRODUCTION

Over the last years, flexible, stretchable and conformable electronics have gained tremendous attention due to their exceptional attributes like the degree of deformation, a conformability with any body contour and the lightweight character. Hence, they play a pivotal role in the development and fabrication of novel and miniaturized sensor devices. Notably applications for human health monitoring have benefited from these features ranging from strain gauges for detection of the respiratory rate, human body temperature sensors to capacitive pressure sensors for wound monitoring [1–3]. These achievements are enabled by two key factors. On the one hand the advancement of manufacturing techniques towards resource-efficient additive fabrication methods beyond clean room environments have facilitated a precise patterning of microscaled sensor structures. The best-known representatives of such printing approaches are inkjet printing [2, 4] and screen printing [5, 6]. In consideration of the persistent trend for miniaturization of electronic devices, innovative technologies for high-precision printing are also subject of research. Here, electrohydrodynamic printing (EHD) [7–9] is of special interest due to its compatibility with various ink- and substrate materials which exceeds the opportunities

of other methods significantly. In particular the substrate materials are of paramount importance for shape-adjustable sensors which constitute the second factor of success for fabrication of stretchable electronic devices. For applications in the field of human health monitoring the substrates have to be biocompatible and hyperelastic for an optimal adaption on the skin surface. In general, polydimethylsiloxane (PDMS) [1, 10] as well as thermoplastic polyurethane [5, 11, 12] are commonly used materials for such purposes. Nevertheless, they are accompanied by divergent material properties in contrast to the antagonistic stress-strain behavior of metals like copper or silver utilized for embedding conductive and functional traces within the stretchable sensors. These conditions can be responsible for material destruction and delamination processes among substrates and metallic traces in case of strong deformations. A broad knowledge about the material behavior of TPU is therefore crucial. Hyperelastic or rather rubber like materials cannot be described by a linear elastic stress-strain curve as schematically illustrated in Fig. 1.
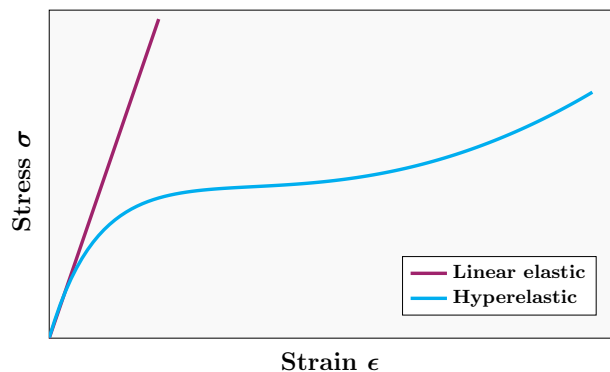

Fig. 1: Schematic representation of the stress-strain curves for linear elastic and hyperelastic materials.

Kumar and Rao [13] define a material as hyperelastic in case of the presence of an elastic strain energy density function (W) which represents a scalar function of the corresponding strain deformation tensors. Its derivatives define the relating stress components in consideration of the strain components. As a result, constitutive models of hyperelastic materials come along with material nonlinearity as well as large deformations. Thus, the fundamentals of frequently applied hyperelastic material models are discussed in detail within the following

section. With regard to the sensor design realized in this work, the models are analyzed towards an application of TPU.

II. PHENOMENOLOGICAL HYPERELASTIC MATERIAL MODELS

Thermoplastic polyurethane is appropriate for various flexible and shape-adjustable sensor applications owing to its low elastic modulus and a high bulk modulus, respectively [13]. There are several existing phenomenological hyperelastic material models for description of the relating material behavior of TPU or rather rubber materials [14]. In a first step, the scalar elastic strain energy density function (W) is set, which is either dependent on strain tensors (e.g. right or left Cauchy - Green) or on the invariants of the strain tensors (I_1, I_2, I_3). A third option is the direct correlation with the principal stretches $(\lambda_1, \lambda_2, \lambda_3)$ [15]. The hyperelastic material models are classified according to stretch- or invariant-based versions in the present work which is represented in Fig. 2.
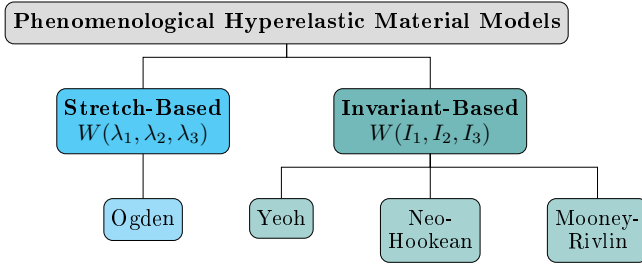

Fig. 2: Classification of phenomenological hyperelastic material models. Adapted from [14, 15].

In a first instance, a curve fitting for the stretch-based Ogden (4th order) model as well as the invariant-based Yeoh, Neo-Hookean and the Mooney-Rivlin (5-parameter) model is implemented via MATLAB what is validated against existing stress-strain measurement data [16]. The results of the curve fitting are prefixed in Fig. 3 for a better transparency of the subsequent model descriptions. Beside these models, other variations of lower orders, like the Ogden model of 3rd order
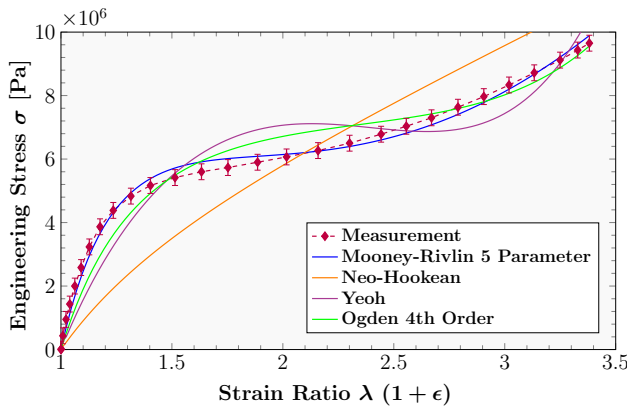

Fig. 3: Comparison of hyperelastic material models for description of TPU by means of MATLAB.

and the 2 parameter Mooney-Rivlin model, are also investigated. The results gained through these approaches do not meet the measurement data satisfactorily. Therefore, they are not further considered within this paper. In the following sections the four hyperelastic models which are of special interest are introduced in more detail.

A. Ogden Model

According to Fig. 2, the Mooney-Rivlin, Neo-Hookean and the Yeoh approaches are defined as invariant-based versions of the relating strain energy density functions W. In contrast to these models, the strain energy density function W_O of the Ogden model is defined in terms of principal stretches λ [17]. Here, the so-called Ogden 4th order model is applied for fitting the available measurement data. The strain energy density function W_O for the Ogden model is described by (1) with regard to the three principal stretches λ_i $(i = 1, 2, 3)$:

$$W_O (\lambda_1, \lambda_2, \lambda_3) = \sum_{i=1}^{n=4} \frac{2\mu_i}{\alpha_i^2} (\lambda_1{}^{\alpha_i} + \lambda_2{}^{\alpha_i} + \lambda_3{}^{\alpha_i} - 3)$$
$$+ \sum_{i=1}^{n=4} \frac{1}{D_i} (J_{el} - 1)^{2i} \tag{1}$$

where J_{el} expresses the elastic volume ratio and n represents the order of the Odgen model. The relating hyperelastic constants are described by μ_i, α_i and D_i with $(i = 1, 2, ..., n)$. While μ_i is connected to the initial shear modulus and has the unit of stress, α_i and D_i are dimensionless. The hardening or rather softening exponent of the model is given by α_i [18]. With regard to Fig. 3 is can be noted that this material model approximates the measurement data only moderately.

B. Yeoh Model

In case of the realization of highly stretchable sensors with large strain rates the phenomenological invariant-based Yeoh model can be particularly appropriate. It is usually used for description of of almost incompressible and non-linear materials. The corresponding strain energy density function W_{Yeoh} is given by (2) where C_{10}, C_{20} or rather C_{30} denote the material constants and I_1 is the first invariant [19].

$$W_{Yeoh} = C_{10} (I_1 - 3) + C_{20} (I_1 - 3)^2$$
$$+ C_{30} (I_1 - 3)^3 \tag{2}$$

Even though the Yeoh model has the character of a reduced form of the original hyperelastic material model, a description of the hyperelastic material behavior of TPU can be determined in principle. Nonetheless, the convergence of the results is comparable to the previously introduced Ogden model of 4th order (cf. Fig. 3) which is therefore partially recommended for the specification of TPU.

C. Neo-Hookean Model

Beside the Ogden and Yeoh approaches, the Neo-Hookean model is commonly utilized for description of hyperelastic materials. Its working strain range is up to 30% [13]. This model constitutes the simplest form of these hyperelastic material models. It represents a reduced form of the polynomial Mooney–Rivlin model and is solely dependent on the first invariant I_1, the material constants C_{10} and D_1. The expression D_1 can alternatively be described as $2/\kappa_{Neo}$, which is linked to the elastic volume ratio J_{el} [19]. For the invariant-based Neo-Hookean model the relating strain energy density function W_{Neo} is given by (3):

$$W_{Neo} = C_{10}\left(I_1 - 3\right) + \frac{\kappa_{Neo}}{2}\left(J_{el} - 1\right)^2 \tag{3}$$

The corresponding bulk modulus for the Neo-Hookean model κ_{Neo} [20] is described by the following term (4):

$$\kappa_{Neo} = \frac{4\left(\nu + 1\right)C_{10}}{3\left(1 - 2\nu\right)} \tag{4}$$

In consideration of all graphical results of the hyperelastic material models in Fig. 3 it can be noted that the Neo-Hookean model is only restrictedly suitable for description of TPU. It meets the measurement data insufficiently and is more appropriate for fitting measurement data at relatively low strain rates what is also underpinned by Kumars and Raos [13] assertion concerning the working strain range.

D. Mooney-Rivlin Model

The invariant-based 2, 3, 5 and 9 parameter Mooney-Rivlin models, which can be traced back to the pioneering works of Mooney and Rivlin [21, 22], are frequently utilized constitutive versions for analysis of hyperelastic or rubber like materials such as TPU. In this paper, the investigations are focussed on the 5 parameter Mooney-Rivlin model where the elastic strain energy density function W_{MR} is defined by three invariants of strain I_1, I_2 and I_3. In consideration of the incompressibility of TPU, the third invariant becomes one ($I_3 = 1$) [16]. As a result, the elastic strain energy density function W_{MR} can be interpreted as a linear combination with two invariants I_1 and I_2 of the corresponding left Cauchy–Green deformation tensor [23]. With regard to the specific case of an uniaxial load, W_{MR} can be described through (5):

$$\begin{aligned} W_{MR} = {} & C_{10}\left(I_1 - 3\right) + C_{01}\left(I_2 - 3\right) \\ & + C_{20}\left(I_1 - 3\right)^2 + C_{02}\left(I_2 - 3\right)^2 \\ & + C_{11}\left(I_1 - 3\right)\left(I_2 - 3\right) \\ & + \frac{\kappa_{MR}}{2}\left(J_{el} - 1\right)^2 \end{aligned} \tag{5}$$

where I_1 as well as I_2 denote the invariants and C_{01}, C_{10}, C_{11}, C_{02}, C_{20} express the relating material constants. J_{el} describes

the elastic volume ratio and κ_{MR} the bulk modulus, respectively [13]. Furthermore, the relation between the invariants I_1 as well as I_2 and the strain ϵ or rather strain ratio $\lambda = 1 + \epsilon$ are given by (6) and (7):

$$I_1 = \left(\lambda^2 + \frac{2}{\lambda}\right) \tag{6}$$

$$I_2 = \left(2\lambda + \frac{1}{\lambda^2}\right) \tag{7}$$

A relating extraction of the material constants C_{01}, C_{10}, C_{11}, C_{02} and C_{20} based on the elastic strain energy density function W_{MR} is also realized by means of MATLAB. Tab. 1 summarizes these results as preparatory work for a subsequent implementation of them into the simulation models. In addition, the bulk modulus κ_{MR} is also analyzed and connected with the Poisson's ratio ν [20] by (8):

$$\kappa_{MR} = \frac{4\left(\nu + 1\right)\left(C_{10} + C_{01}\right)}{3\left(1 - 2\nu\right)} \tag{8}$$

As a consequence, the subsequent stress-strain relation σ_{MR} can be derived for the phenomenological invariant-based 5 parameter Mooney-Rivlin model that can be calculated by (9):

$$\begin{aligned} \sigma_{MR} = 2\left(1 - \lambda^{-3}\right) \Big(& \lambda C_{10} + 2C_{20}\lambda\left(I_1 - 3\right) \\ & + C_{11}\lambda\left(I_2 - 3\right) + C_{01} + 2C_{02}\left(I_2 - 3\right) \\ & + C_{11}\left(I_1 - 3\right)\Big) \end{aligned} \tag{9}$$

A comparison of all fitting curves illustrated in Fig. 3 leads to the conclusion that the 5 parameter Mooney-Rivlin model meets the measurement data [16] of hyperelastic TPU best, what makes it to a promising approach. Therefore, the Mooney-Rivlin approach is subsequently utilized within the COMSOL models for the determination of an interaction between hyperelastic TPU and embedded copper structures or rather in connection with the design and development of resistive and capacitive shape-adjustable sensors.

Tab. 1: Extracted material constants of the TPU based on the 5 parameter Mooney-Rivlin model.

Parameter	Value	Unit
C_{10}	-3.281×10^6	Pa
C_{01}	8.399×10^6	Pa
C_{11}	3.538×10^5	Pa
C_{20}	1.140×10^{-4}	Pa
C_{02}	-4.086×10^{-13}	Pa
κ	5.085×10^8	Pa
ν	0.490	–

III. COMSOL MODELING

After a comprehensive introduction to phenomenological hyperelastic material models in the previous section along with the application of these approaches on TPU, it has turned out that the 5 parameter Mooney-Rivlin model represents the most appropriate method for the description of the relating material behavior. Consequently, it is implemented within COMSOL models for investigation of $100\,\mu m$ thick TPU sheets with embedded filigree copper structures serving as resistive and capacitive sensor elements or rather electrodes.

In a first step, 3D COMSOL models are built up by means of the *Solid Mechanics* module for realization of rudimental resistive sensors or rather strain gauges. This procedure allows the investigation of geometric nonlinearities and large deformations of the TPU substrates as well as an implementation of user defined hyperelastic materials based on the correlating strain energy density function W_{MR} introduced in section II-D. A variation of the copper trace geometry is used for shape optimization of the embedded linear elastic structures. In this way, considerable strain rates of TPU are achieved without disruption of the copper lines and meanders or delamination of the TPU material. To characterize the resistance behavior of the strain gauges, the *Electric Currents* module and the *Mathematics* module with the *Deformed Geometry* interface are also utilized within the simulation model. Moreover, two designs of a shape-adjustable resistive and capacitive sensor device are developed and implemented in COMSOL which are presented in more detail in the sections III-B and III-C.

A. Geometry Optimization of Functional Traces

A numerical investigation of TPU with embedded copper structures is reasonable for a profound understanding of an interaction between the antagonistic material behaviors of TPU and the linear elastic material. Hence, the dependence and influence of different copper geometries are examined within this work. Of paramount importance are in particular the resulting stress-strain characteristics and the change in resistance during deformation of the strain gauges. Philippin et al. [16] have examined similar aspects in a former publication for fabrication of stretchable PCBs. In this context, strong deformations of about 50% strain without material failure could be evidenced by numerical simulations and are confirmed experimentally by measurements. Following these findings, three different copper trace geometries are analyzed in the present work consisting of straight copper lines, U-shaped meander structures and rectangular traces. Fig. 4(a)-(f) illustrates the simulation results. In Fig. 4(a)-(c) the geometric variations are shown in their initial state. Contrary to that, Fig. 4(d)-(f) presents the deformed TPU sheets at 40% strain. In general, red areas indicate high acting stresses whereas blue segments are less affected by the stresses. This leads to the conclusion, that meanders and rectangular copper traces are more suitable for stretchable sensor devices than straight copper geometries. The consideration of the results is mandatory for an application

of large strain rates of conductive copper traces and also of great importance for lead resistances of stretchable capacitive sensors under dynamic conditions (cf. section III-C).
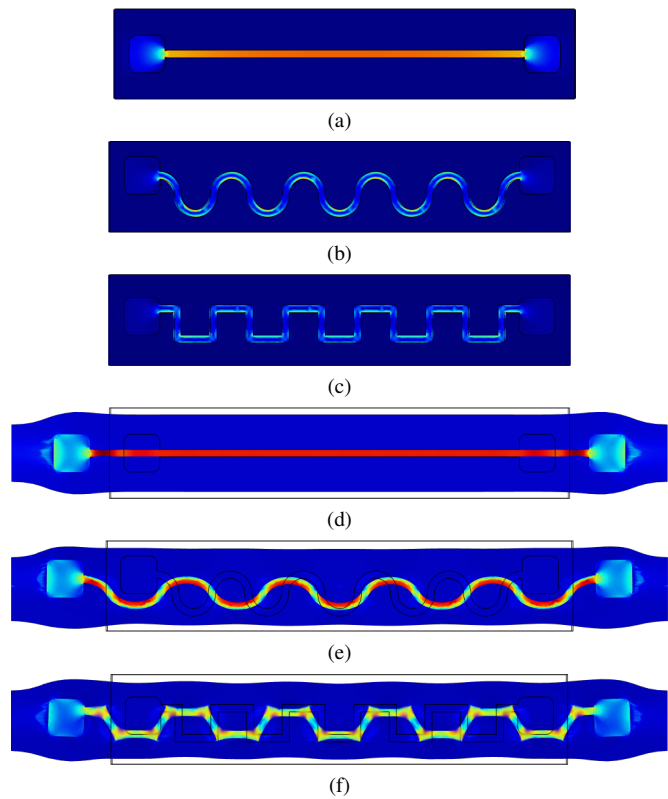

Fig. 4: COMSOL simulation for shape optimization of TPU with functional copper structures: (a) Straight copper trace, (b) meander of 180°, (c) rectangular shape of metallic structures in the initial state and (d)-(f) all three copper trace geometries at 40% strain.

Moreover, COMSOL has enabled the derivation and quantification of occurring average von Mises stresses σ_M (cf. Fig. 4) and the normalized initial resistances $R_{0,norm.}$ of the three different copper geometries. The results are summarized in Tab. 2 and are also mentioned in the publication of Philippin et al. [8]. In particular, the rectangular copper traces (see Fig. 4(c)) have shown promising results what is consequently the fundament for the design of a resistive sensor in section III-B.

Tab. 2: Comparison of the normalized initial resistances and stresses dependent on the copper geometries.

Geometry		$R_{0,norm.}$	σ_M
Straight		100%	100%
Meander 180°		157%	90%
Rectangular		291%	26%

Beside the analysis of mechanical stresses, an electrical characterization of the embedded copper traces is also of importance towards the lead resistance behavior of stretchable capacitive sensors. The resistance behavior of relating copper meanders is shown in Fig. 5. Strain rates up to 60% has shown appropriate simulation results which are in excellent approximation to the measurement data [16].
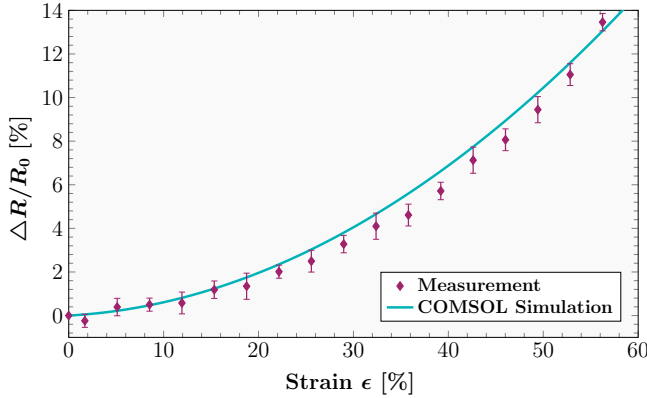

Fig. 5: Relative change in resistance $\triangle R/R_0$ of the strain gauge: Comparison of simulation and measurement results for strain rates up to 60%.

The results gained through the geometry optimization procedure by means of COMSOL are utilized afterwards for the design of a prototypical resistive and shape-adjustable sensor device. Here, the beneficial properties of rectangular metallic copper structures pursuant to the findings in Tab. 2 are applied.

B. Shape-Adjustable Resistive Sensor Device

For the design and FEM simulation based development of a stretchable resistive sensor, a $100\,\mu m$ thick TPU sheet with a length of $3800\,\mu m$ and a width of $2000\,\mu m$ is initially implemented via the *Geometry* interface in COMSOL, which is illustrated in Fig. 6. In this substrate rectangular copper meanders with a line width of $50\,\mu m$ are embedded which are connected to feed lines and squared electrodes. Relating to the introduced Mooney-Rivlin model, the extracted material constants of Tab. 1 are inserted in the *Hyperelastic Material* node of the *Solid Mechanics* module. The uniaxial displacement of the TPU sheet is prescribed over a piecewise function to create a ramp for elongation and relaxation of the sensor device as well as to reach an adequate hysteresis behavior. According to the sensor design in Fig. 6(a) and the FEM model illustrated in Fig. 6(b), a shape adjustable resistive sensor is successfully realized which allows a strain rate of more than 15%. Such a stress-strain characteristic could be quite suitable with regard to wearable applications for the purpose of health monitoring or motion detection. Beside resistive sensors, capacitive wearable devices are also of importance for human health applications. Therefore, an additional sensor model is introduced within the following section III-C.
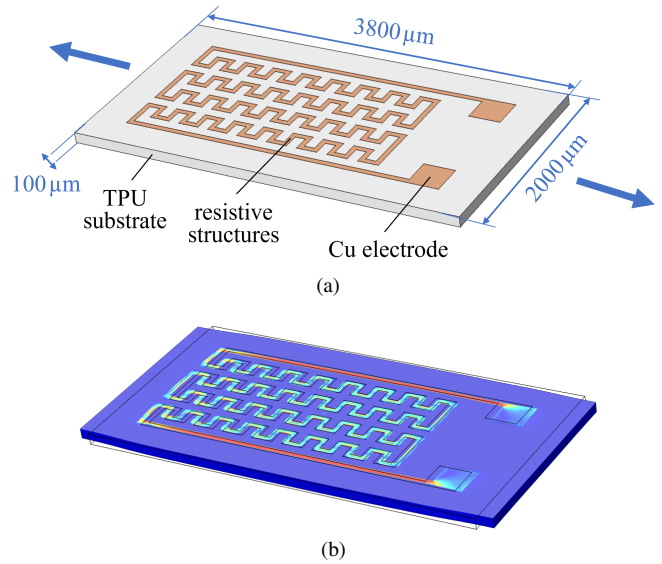

Fig. 6: Resistive sensor: (a) Sensor design based on TPU with rectangular copper traces and (b) FEM model at 15% strain under an uniaxial load.

C. Shape-Adjustable Capacitive Sensor Device

The second sensor design implemented within this work is a capacitive sensor (cf. Fig. 7(a)-(b)). Analogously to the procedure explained in section III-B, a FEM model is built up with a TPU substrate of $3500\,\mu m$ x $900\,\mu m$ x $100\,\mu m$. The capacitive copper traces have also a structure width of $50\,\mu m$. Despite the integrated feed lines have experienced relatively high stresses for strains of the hyperelastic TPU above 10%, there is no destruction or delamination of the material complex observable up to considerable deformations of 35%. Such a promising strain characteristic can therefore pave the way to entirely new shape-adjustable sensor applications.
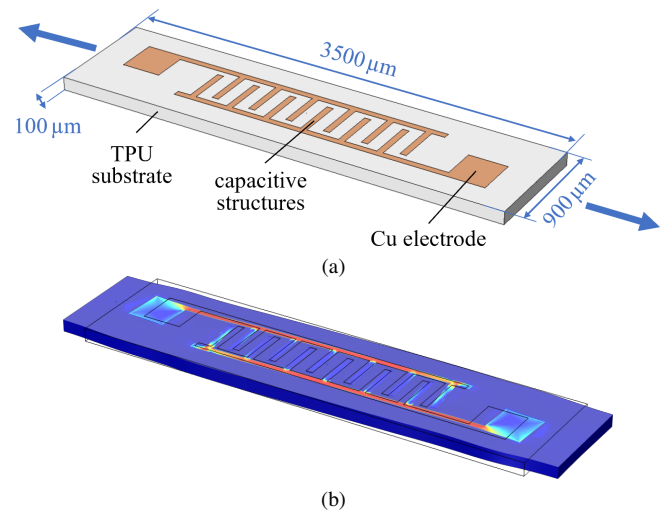

Fig. 7: Capacitive sensor: (a) Sensor design based on TPU with copper traces and (b) FEM model at 15% strain under an uniaxial load.

D. Meshing of Sensor Models

Both introduced simulation models of the shape-adjustable resistive and capacitive sensor devices are governed by large strain rates and displacements. This aspect necessitates the selection and adjustment of the governing mesh elements to gain appropriate and precise simulation results. The mesh of a FEM model constitutes the spatial discretization of its relating geometry and is therefore of paramount importance. Hence, the size of the mesh elements has to be chosen in such a manner that the element quality is reasonable and, at the same time, the computational time is moderate also for filigree meshes. In the present work, all simulations of the resistive and capacitive sensor devices are performed on three different meshes with normal (96.533 and 24.889 elements), fine (165.004 and 40.483 elements) and finer (370.596 and 101.378 elements) structure, respectively. In both cases, the finer mesh (schematically illustrated for the capacitive sensor in Fig. 8) is selected because the simulations has shown more appropriate results in the required computational time compared to the other meshes with a lower number of elements.
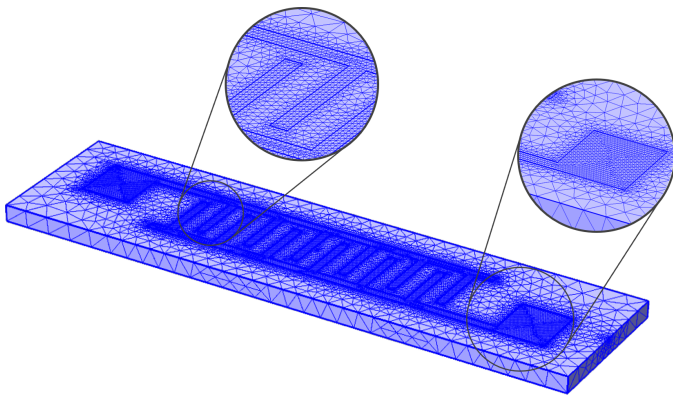

Fig. 8: Meshing of the capacitive sensor with finer structure.

IV. Conclusion

In this work, FEM models of shape-adjustable resistive and capacitive sensors based on stretchable and hyperelastic TPU substrates with functional copper elements are introduced successfully aiming the development of novel sensor devices for human health monitoring. For that purpose, relevant fundamentals of phenomenological stretch- and invariant-based hyperelastic material models - with focus on the 5 parameter Mooney-Rivlin model - are discussed initially. Potentials for shape optimization of linear elastic copper structures for an improved stress-strain behavior of the devices have been highlighted complementarily. The findings gained through these analysis are implemented within the FEM models of the resistive and capacitive sensors to achieve best possible results. In conclusion, the numerical analysis by means of COMSOL Multiphysics® has proven an uniaxial deformation of the sensors up to 35% without loss of functionality or delamination of the materials.

References

[1] A. A. Al-Halhouli, L. Al-Ghussain, S. El Bouri, F. Habash, H. Liu, and D. Zheng, "Clinical evaluation of stretchable and wearable inkjet-printed strain gauge sensor for respiratory rate monitoring at different body postures," *Appl. Sci.*, vol. 10, no. 2, 2020, Art. no. 480 doi:10.3390/app10020480.

[2] S. Ali, S. Khan, and A. Bermak, "Inkjet-Printed Human Body Temperature Sensor for Wearable Electronics," *IEEE Access*, vol. 7, pp. 163981–163987, 2019, doi:10.1109/ACCESS.2019.2949335.

[3] D. T. N. Nga, G. Mattana, V.T. Thu, R. Roussel, and B. Piro, "A simple flexible printed capacitive pressure sensor for chronic wound monitoring," *Sensor Actuat. A-Phys.*, vol. 338, 2022, Art. no. 113490, doi:10.1016/j.sna.2022.113490.

[4] Q. J. Liew, A. S. A. Aziz, H. W. Lee, M. W. Lee, H. F. Hawari, and M. H. Md Khir, "Inkjet-Printed Flexible Temperature Sensor Based on Silver Nanoparticles Ink," *Eng. Proc.*, vol. 2, no. 1, 2020, doi:10.3390/ecsa-7-08216.

[5] J. Ahmad, J. Sidén, and H. Andersson, "Stretchable Pressure Sensor Using Thermoplastic Polyurethane and Conductive Inks," in *Proc. IEEE Sensors*, 2021, doi:10.1109/SENSORS47087.2021.9639852.

[6] A. Moorthi, B. B. Narakathu, A. S. G. Reddy, A. Eshkeiti, H. Bohra, and M. Z. Atashbar, "A novel flexible strain gauge sensor fabricated using screen printing," in *Proc. 2012 Sixth Intern. Conf. on Sens. Techn. (ICST)*, pp. 765–768, 2012, doi:10.1109/ICSensT.2012.6461780.

[7] N. Philippin, I. Kuehne, and G. Schrag, "Electric-Field-Assisted Printing Technology for Enhanced Patterning of Micro- and Nanostructures," *MikroSystemTechnik Kongress 2023*, pp. 205–210, 2023, ISBN: 978-3-8007-6203-3.

[8] N. Philippin, I. Kuehne, and G. Schrag, "Conformable Electronics with Conductive Silver Structures by Electrohydrodynamic Printing," *IEEE J. on Flex. Electr. (J-FLEX)*, 2024, doi:10.1109/JFLEX.2024.3420263.

[9] N. Mkhize, and H. Bhaskaran, "Electrohydrodynamic Jet Printing: Introductory Concepts and Considerations," *Small Science*, vol. 2, no. 2, 2022, Art. no. 2100073, doi:10.1002/smsc.202100073.

[10] Z. Sun, S. Yang, P. Zhao, J. Zhang, Y. Yang, X. Ye, X. Zhao, N. Cui, Y. Tong, Y. Liu, X. Chen, and Q. Tang, "Skin-like Ultrasensitive Strain Sensor for Full-Range Detection of Human Health Monitoring," *ACS Appl. Mater. Interfaces.*, vol. 12, no.11, pp. 13287–13295, 2020, doi:10.1021/acsami.9b21751.

[11] M. M. Ali, D. Maddipatla, B. B. Narakathu, A. A. Chlaihawi, S. Emamian, F. Janabi, B. J. Bazuin, and M. Z. Atashbar, "Printed strain sensor based on silver nanowire/silver flake composite on flexible and stretchable TPU substrate," *Sens. Actuators A: Phys.*, vol. 274, pp. 109–115, 2018, doi:10.1016/j.sna.2018.03.003.

[12] C. S. Smith, K. Sondhi, B. Jimenez, Z. H. Fan, T. Nishida, and D. P. Arnold, "Screen-Printed Inductive Silver Ink Strain Sensor on Stretchable TPU Substrate," in *Proc. IEEE 70th Electron. Compon. Technol. Conf.*, pp. 2325–2329, 2020, doi:10.1109/ECTC32862.2020.00362.

[13] N. Kumar, and V.V. Rao, "Hyperelastic Mooney-Rivlin Model: Determination and Physical Interpretation of Material Constants," *MIT Int. J. Mech. Eng.*, vol. 6, no. 1, pp. 43–46, 2016.

[14] H. He, Q. Zhang, Y. Zhang, J. Chen, L. Zhang, and F. Li, "A comparative study of 85 hyperelastic constitutive models for both unfilled rubber and highly filled rubber nanocomposite

material," *Nano Mat. Science*, vol. 4, no. 2, pp. 64–82, 2022, doi:10.1016/j.nanoms.2021.07.003.

[15] P. Steinmann, M. Hossain, and G. Possart, "Hyperelastic models for rubber-like materials: consistent tangent operators and suitability for Treloar's data," *Arch. Appl. Mech.*, vol. 82, pp. 1183–1217, 2022, doi:10.1007/s00419-012-0610-z.

[16] N. Philippin, A. Schreivogel, I. Kuehne, and J. Kostelnik, "Electronics of a new dimension - Potentials of stretchable foil systems for development of interactive microimplants.," *Proc. EBL - Elektronische Baugruppen und Leiterplatten 2020*, pp. 68–73, 2020, ISBN: 978-3-8007-5185-3.

[17] P.S. Lin, O. Le Roux de Bretagne, M. Grasso, J. Brighton, C. StLeger-Harris, and O. Carless, "Comparative Analysis of Various Hyperelastic Models and Element Types for Finite Element Analysis," *Designs*, vol. 7, no. 6, 2023, Art. no. 135, doi:10.3390/designs7060135.

[18] S. Yan, D. Jia, Y. Yu, L. Wang, Y. Qiu, and Q. Wan, "Novel strategies for parameter fitting procedure of the Ogden hyperfoam model under shear condition," *Eur. J. Mech. A-Solid.*, vol. 86, 2021, Art. no. 104154, doi:10.1016/j.euromechsol.2020.104154.

[19] H.-D. Nguyen, and S.-C. Huang "The Uniaxial Stress–Strain Relationship of Hyperelastic Material Models of Rubber Cracks in the Platens of Papermaking Machines Based on Nonlinear Strain and Stress Measurements with the Finite Element Method," *Materials*, vol. 14, no. 24, 2021, Art. no. 7534, doi:10.3390/ma14247534.

[20] W. Shi, G. Lui, and Z. Chen, "Effects of the bulk compressibility on rubber isolator's compressive behaviors," *Adv. Mech. Eng.* , vol. 9, no. 5, pp. 1–12, 2017, doi:10.1177/1687814017699352.

[21] M. Mooney, "A Theory of Large Elastic Deformation," *J. Appl. Phys.*, vol. 11, no. 9, pp. 582–592, 1940, doi:10.1063/1.1712836.

[22] R.S. Rivlin, "Large elastic deformations of isotropic materials. I. Fundamental concepts," *Philos. Trans. R. Soc., Series A, Math. Phys. Sci.*, vol. 240, no. 822, pp. 459–490, 1948, doi:10.1098/rsta.1948.0002.

[23] A.N. Jadhav, S.R. Bahulikar, and N.H. Sapate, "Comparative Study of Variation of Mooney-Rivlin Hyperelastic Material Models Under Uniaxial Tensile Loading," *Int. J. of Adv. Res. and Inn. Ideas in Educ.*, vol. 2, no. 4, pp. 212–216, 2016.